

Direct inelastic scattering of $^{14}\text{N} + ^{12}\text{C}$ in a three-dimensional time-dependent Hartree-Fock scheme

R. Y. Cusson*

Physics Department, Duke University, Durham, North Carolina 27706

J. A. Maruhn†

Oak Ridge National Laboratory † Oak Ridge, Tennessee 37830

H. W. Meldner§

Lawrence Livermore Laboratory, Livermore, California 94550

(Received 7 April 1978; revised manuscript received 24 July 1978)

Momentum space three-dimensional time-dependent Hartree-Fock (TDHF) calculations are performed for $^{12}\text{C} + ^{14}\text{N}$ and $^{16}\text{O} + ^{16}\text{O}$ collisions. The potential is the simplified Skyrme interaction which gives the single-particle potential $v_N(r) = -a\rho(r) + b\rho^2(r)$, and includes the direct part of the Coulomb interaction. We use a predictor-corrector method to step in time and a fast Fourier transform (FFT) method to compute the kinetic energy in momentum space. Three types of events are obtained: vibrational instability scattering at low impact parameters b , near orbiting at medium b values, and rotational instability scattering beyond that. The discussion points out that further improvements will require a fusion window and quantal corrections for angular and energy uncertainties which go beyond the TDHF method.

[NUCLEAR REACTIONS $^{14}\text{N}(112\text{ MeV}) + ^{12}\text{C}$, $^{16}\text{O}(128\text{ MeV}) + ^{16}\text{O}$, calculated deflection functions using time-dependent Hartree-Fock approximation.]

I. INTRODUCTION

The results of inelastic heavy-ion collisions,¹⁻³ where the projectile energy per nucleon E_t/A_p is substantially above the Coulomb barrier, have been described⁴ as collisions of two bodies moving along classical trajectories with elastic and frictional forces. This interpretation relies on the range of angular momenta l participating in the two-body collision being several hundred times \hbar where

$$l = \mu v b, \quad v = \sqrt{\left(\frac{2}{m} \frac{E_t}{A_p}\right)},$$

and μ is the reduced mass of target (t) and projectile (p), b is the impact parameter. More recently, measurements of $d^2\sigma/d\Omega dE$ have been performed⁵⁻¹⁰ for lighter systems with angular momenta up to 25–50 \hbar . There, the inelastic transfer angular distributions with a given Q -value slice (partially energy integrated $d^2\sigma/d\Omega dE$) show mainly an exponential decrease with increasing laboratory angle. The exponential behavior can be heuristically explained¹¹ by using the Blair diffuse surface model¹² and appears to be at odds with the semiclassical interpretation of Wilczynski.

We calculate in this paper the energy loss and deflection angle for the reactions $^{12}\text{C} + ^{14}\text{N}$ and $^{16}\text{O} + ^{16}\text{O}$ at 8 MeV/nucleon laboratory bombarding energy and for the impact parameters of interest. This

calculation is described in Sec. II, beginning with the use of the fast Fourier transform (FFT) algorithm¹³ to connect coordinate and momentum space. We then describe the predictor-corrector method¹⁴ used to solve the time-dependent Schrödinger equation

$$i\hbar \frac{\partial \psi_\lambda}{\partial t} = h\psi_\lambda.$$

Next we describe the initial wave functions needed to solve the equation; they are plane waves times harmonic oscillator states. Then comes the Coulomb field calculation¹⁵; it avoids most of the image problems usually encountered when using a long-range force and the FFT periodic boundary condition. Other details of the Coulomb orbits are also presented. A discussion of the symmetries imposed in order to shorten the computation time follows and leads to the topic of the grid dimensions; the various considerations connected with this are briefly mentioned. We end the section by giving the formulas for the computation of currents, in addition to collective and thermal energies.

The results are presented in Sec. III. We begin by showing density and velocity plots for three cases: (i) vibrational scattering at low impact parameter b , (ii) capture or orbiting for medium b values, and (iii) rotational scattering at high b 's. These illustrations are taken from the two reac-

tions studied in this paper: $^{16}\text{O} + ^{16}\text{O}$ and $^{14}\text{N} + ^{12}\text{C}$ at bombarding energies $E_i(^{16}\text{O})/16 = 8 \text{ MeV} = E_i(^{14}\text{N})/14$. The first reaction was chosen because of the simple closed shell nature of ^{16}O and the target-projectile symmetry which allows a faster calculation. The second reaction was studied in order to compare with some recent experimental data¹¹ from ORNL. Several striking similarities of these calculations with the hydrodynamic scattering modes of classical water droplets are noted even though no two-body viscosity term is ever considered explicitly. We then proceed to a more detailed presentation of the various important physical quantities such as the deflection angle and the energy loss (Q value) as a function of the incoming total center-of-mass (c.m.) orbital angular momentum l . Then we discuss the energy dependence of the $^{16}\text{O} + ^{16}\text{O}$ reaction at a fixed impact parameter $b = 4 \text{ fm}$, in the energy range $4 \text{ MeV} \leq E_i/A_p \leq 36 \text{ MeV}$.

The discussion also suggests possible correction to the time-dependent Hartree-Fock (TDHF)¹⁶⁻¹⁹ method for quantal effects.^{20,21} We point out that one can obtain phenomenological expressions for the direct inelastic cross section which yield approximate exponentially decaying inelastic angular distributions for small l values and the classical results for high l values.

II. CALCULATION

This section first presents a brief derivation of the TDHF equations. Our solution is then dis-

$$\begin{aligned} i\hbar \frac{\partial}{\partial t} \rho(r, r') = & \frac{\hbar^2}{2m} (\nabla^2 - \nabla'^2) \rho(r, r') + [\bar{v}(r) - \bar{v}(r')] \rho(r, r') - \int d^3r'' \rho(r, r'') [v(r - r'') - v(r' - r'')] \rho(r, r') \\ & + \int d^3r'' [v(r - r'') - v(r' - r'')] g^{(2)}(r, r''; r', r''), \end{aligned} \quad (2.3)$$

where \bar{v} denotes the average potential

$$\bar{v}(r) = \int d^3r' v(r - r') \rho(r', r'). \quad (2.4)$$

On the right side of Eq. (2.3) the second term describes scattering from the average potential, followed by the corresponding exchange term, whereas the last expression denotes residual two-body interactions. In ordinary macroscopic fluid dynamics this last term has its analogy in the collision term of the Boltzmann equation; it is responsible for damping effects such as viscosity, whereas the potential scattering is usually negligible for macroscopic fluids.

In nuclear collisions, on the other hand, the average potential is strongly space and time dependent, while collisions are inhibited by the Pauli

principle. We also mention various other points such as the initial conditions, the Coulomb potential, the symmetries, and the grid properties; finally, we outline the calculation of the currents, the thermal energy, and the collective energy.

A. The TDHF equations

One possible derivation of the TDHF equations, which is particularly useful for understanding the underlying physical ideas, starts from the equation for the one-particle density matrix within the Bogoliubov-Born-Green-Kirkwood-Yvon (BBGKY)²² hierarchy

$$\begin{aligned} i\hbar \frac{\partial}{\partial t} \rho(r, r') = & -\frac{\hbar^2}{2m} (\nabla^2 - \nabla'^2) \rho(r, r') \\ & + \int d^3r'' [v(r - r'') - v(r' - r'')] \\ & \rho^{(2)}(r, r''; r', r''). \end{aligned} \quad (2.1)$$

Here the interaction between the particles was assumed to be expressible as an interaction potential $v(r - r')$, and $\rho^{(2)}$ is the two-particle density matrix, which can also be expressed in terms of the one-particle density matrix and a two-particle correlation function $g^{(2)}$:

$$\begin{aligned} \rho^{(2)}(r, r''; r', r'') = & \rho(r, r') \rho(r'', r'') \\ & - \rho(r, r'') \rho(r', r') \\ & + g^{(2)}(r, r''; r', r''). \end{aligned} \quad (2.2)$$

Inserting this expression in Eq. (2.1), one obtains

principle, at least at low energies.

It thus appears useful to study the approximation obtained by assuming $g^{(2)} \equiv 0$. This will lead to the TDHF equations. For practical calculations, however, we have to make two further assumptions: (1) We use a zero-range density-dependent effective interaction of the simplified Skyrme type,^{17,19} so that the average potential becomes

$$\bar{v}(r) = -a\rho(r, r) + b\rho^2(r, r); \quad (2.5)$$

a and b are determined such as to yield an equilibrium density of 0.145 fm^{-3} and a binding energy of -15.85 MeV for nuclear matter. The resulting incompressibility κ is 368 MeV . (2) We assume a representation of $\rho(r, r')$ in terms of single-particle wave functions of the form

$$\rho(r, r') = \sum_{\lambda} n_{\lambda} \psi_{\lambda}(r) \psi_{\lambda}^*(r'), \quad (2.6)$$

with the occupation probabilities n_{λ} time independent. This is a slight generalization of the usual single Slater determinant and allows partial occupation of orbitals in order to, e.g., construct spherical initial states for ^{14}N and ^{12}C in a harmonic oscillator basis. The many-body system is then not in a pure state, but this does not give any problems, since the observables may be calculated via the density matrices. The relation between the one- and two-body density matrices is assumed to be the same one as for pure states.

The equation which is actually used in the model is thus

$$i\hbar \frac{\partial}{\partial t} \psi_{\lambda}(r, t) = -\frac{\hbar^2}{2m} \nabla^2 \psi_{\lambda}(r, t) - a\rho(r, t) \psi_{\lambda}(r, t) + b\rho(r, t)^2 \psi_{\lambda}(r, t), \quad (2.7)$$

with the total density

$$\rho(r, t) = \sum_{\lambda} n_{\lambda} \psi_{\lambda}^*(r, t) \psi_{\lambda}(r, t). \quad (2.8)$$

There are as many equations (2.7) as there are n_{λ} differing from zero. Direct substitution of Eqs. (2.6) and (2.7) in Eq. (2.3) yields an identity provided $g^{(2)}$ is neglected and the zero-range Skyrme force is assumed.

B. Fast Fourier transform and the predictor-corrector method

The predictor-corrector method for solving the first order coupled differential equations (2.7) consists of the following two steps:

(1) Predictor of order n :

$$\psi_{\lambda}^i(t + n\Delta t) = \psi_{\lambda}^i(t + (n-1)\Delta t) + \Delta t \sum_{k=0}^{n-1} P_k^n \psi_{\lambda}^i(t + k\Delta t). \quad (2.9)$$

(2) Corrector of order n :

$$\psi_{\lambda}^i(t + q\Delta t) = \psi_{\lambda}^i(t + (q-1)\Delta t) + \Delta t \sum_{k=1}^n C_k^m \psi_{\lambda}^i(t + k\Delta t), \quad 1 \leq q \leq n \quad (2.10)$$

where the label i refers to a particular momentum component. The coefficients P_k^n and C_k^m are chosen by matching the coefficients of the first n terms of the power series expansions on both sides of the equations. The calculations reported here were done with $n=6$. No additional gains are made by going to higher order because each added order requires that one consider an additional time interval Δt for the derivative summation. Thus the time interval over which the power series

must converge increases linearly with the number of terms so that the overall convergence is not improved by adding terms. This effect is independent of numerical errors and depends only on the properties of the Hamiltonian. The label λ refers to the various (orthogonal) orbits which are populated initially.

The potential energy operator is diagonal in coordinate space, while the kinetic energy is diagonal in momentum space. We have used the fast Fourier transform algorithm¹³ to perform the conversion from coordinate to momentum space. For each dimension, we have the relation

$$\psi_{\lambda}(k_l, t) = \sqrt{\left(\frac{\Delta x}{N}\right)} \sum_{m=0}^{N-1} \psi_{\lambda}(x_m, t) e^{-2\pi i m l / N}, \quad (2.11)$$

with $-\frac{1}{2}N \leq l \leq \frac{1}{2}N + 1$. The values of the coordinate x_m and the momentum k_l on their respective grid are given by

$$x_m = m\Delta x, \quad k_l = \frac{2\pi l}{\Delta x N}, \quad \Delta x = 1 \text{ fm}. \quad (2.12)$$

The number of points N was 16 in the x direction, perpendicular to the scattering plane, and $24 = 3 \times 2^3$ in the y and z directions. These dimensions were large enough to accommodate the initial configurations, aligned along the z axis and separated by 10 fm. This grid allows an accuracy of nearly four significant figures on the kinetic energy. However, the potential energy sometimes has a fairly high derivative due to the $\rho^2(r)$ term. Thus, the systematic error in the total energy,

$$E_{\text{tot}} = \sum_{\lambda} n_{\lambda} [\langle T \rangle_{\lambda} - \frac{1}{2} a \langle \rho \rangle_{\lambda} + \frac{1}{3} b \langle \rho^2 \rangle_{\lambda}], \quad (2.13)$$

was larger. The potential energy was computed to an accuracy of about 0.2 MeV. The changes in E_{tot} , which is about -200 MeV, during one time step were less than 0.05 MeV and the overall drift of E_{tot} during a complete event at one impact parameter was less than 0.5 MeV in all cases. The norm is also a good indication of the stability of the calculation. We have found that

$$\sum_l |\psi_{\lambda}(k_l, t)|^2 = \sum_m |\psi_{\lambda}(x_m, t)|^2 \Delta x = 1 \quad (2.14)$$

was conserved to about 10^{-3} for a complete history at one b value. The formulas (2.11), (2.12), and (2.14) are easily extended to three dimensions.

The kinetic energy operator is unbounded in momentum space. This implies a rapidly changing phase

$$\omega_l = \frac{\hbar^2 k_l^2 t}{2m \hbar}.$$

This can be subtracted from the Hamiltonian by setting

$$\psi_\lambda(k_i, t) = C_\lambda(k_i, t) e^{-i\omega t}. \quad (2.15)$$

The Schrödinger equation for C becomes

$$i\hbar \dot{C}_\lambda(k_i, t) = \sum_s \bar{v}(k_i - k_s) e^{i(\omega_i - \omega_s)t} C_\lambda(k_s, t), \quad (2.16)$$

where $\bar{v}(k_i - k_s)$ is the Fourier transform of $\bar{v}(r)$. Since $\bar{v}(\Delta k)$ is not diagonal in momentum space, the sum (2.15) has too many terms in three dimensions. Letting \hat{F} stand formally for the transformation (2.11), the equation (2.15) can be written schematically as

$$\dot{C}_\lambda(k_i, t) = \frac{-i}{\hbar} e^{i\omega_i t} \hat{F} \bar{v}(r) \hat{F}^{-1} e^{-i\omega_s t} C_\lambda(k_s, t). \quad (2.17)$$

Equation (2.17) is the one which was solved using the predictor-corrector method of Eqs. (2.9) and (2.10). The time steps were taken as follows. Given the initial wave function, the initial time derivative \dot{C}_λ is obtained by a subroutine call which performs the manipulations in Eq. (2.17). A first order predictor is then used to obtain $C_\lambda(\Delta t)$ from which $\dot{C}_\lambda(\Delta t)$ is again obtained by Eq. (2.17). This is followed by a first order corrector, then a second order predictor, then two second order correctors ($q=1, 2$), each time computing \dot{C}_λ when a new C_λ is obtained and so on to sixth order. The calculation of Eq. (2.17) represents the major fraction of the computing time because of the FFT involved, even if very fast FFT algorithms are used. A hard wired FFT processor would speed up the calculation very much, but was not available. The wave functions at each step are stored on magnetic tape so that each history can be replayed later when a different quantity is required. The largest time step which gives a stable solution depends on the maximum value of

$$\frac{\hbar^2 k_M^2}{2m},$$

through the approximate empirical relation

$$\frac{\hbar^2 k_M^2}{2m} \frac{\Delta t}{\hbar} \cong 1. \quad (2.18)$$

In three dimensions it is therefore advantageous to truncate the momentum space to those states for which

$$\frac{\hbar^2}{2m} (k_x^2 + k_y^2 + k_z^2) \leq E_{\text{cut}}. \quad (2.19)$$

We choose $E_{\text{cut}} = 125$ MeV in order to ensure adequate convergence at the higher energies studied here ($E/A = 36$ MeV). We also took the value $\Delta t = 1.25$ fm/c as a safe step, reasonably far from the limiting value $\Delta t \cong 1.6$ fm/c predicted by Eq. (2.18). We were not able to increase the step size much above $\Delta t = 1.25$ fm/c, even after truncating

the momentum space further. This appears to be due to a tendency of the zero-range Skyrme force to let the high momentum components of the wave function grow with time. Another limitation on the step size comes from the initial wave function which we now discuss.

C. Initial conditions

The initial wave functions have the form

$$\psi_\lambda(\vec{r}, t=0) = e^{i\vec{k}_\lambda \cdot \vec{r}} \phi_\lambda(\vec{r}), \quad \lambda = 1, \dots, \frac{1}{4}(A_1 + A_2) \quad (2.20)$$

where $\phi_\lambda(r)$ is a harmonic oscillator wave function centered at the c.m. of the cluster to which the orbit λ belongs. The oscillator energy $\hbar\omega$ is chosen to be 37.55 MeV/ $A^{1/3}$, with A the atomic number of a cluster. The wave number \vec{k}_λ is also the cluster value and its orientation depends on the impact parameter b , in the usual way. The cluster momenta are chosen so that the c.m. of the compound system is at rest in the coordinate grid. We also choose the ϕ_λ 's to be real so that they represent approximate stationary eigenstates of the TDHF equations. In order to get an exact stationary state, we would need to do a static HF calculation first. This was not done, and, as a result, there is some initial readjustment of the wave functions as we begin the time stepping. This relatively fast initial change contributes to the present upper limit of $\Delta T = 1.25$ fm/c. Since we put two protons and two neutrons per orbit, the density is computed at each step as

$$\rho(\vec{r}, t) = \sum_{\lambda=1}^{(A_1+A_2)/4} 4 |\psi_\lambda(\vec{r}, t)|^2. \quad (2.21)$$

The initial density is therefore the same as the sum of the densities of the two clusters.

We have used an initial cluster separation of 10 fm. This is enough to ensure that the overlap of the wave functions between different clusters is negligible. The density at the midpoint between the starting cluster is then less than 0.002 times the central density.

D. Coulomb interaction

The Coulomb potential must be computed every time we use Eq. (2.17) to compute \dot{C} , i.e. twice per time step. The potential $\bar{v}(r)$ is

$$\bar{v}(\vec{r}) = -a\rho(\vec{r}) + b\rho^2(\vec{r}) + e^2 \left(\frac{Z}{A}\right)^2 \int d^3r' \frac{\rho(\vec{r}')}{|\vec{r} - \vec{r}'|}. \quad (2.22)$$

The effective charge $(Z/A)^2$ is needed since we do not treat neutrons and protons separately. Computation of the integral over \vec{r}' in coordinate space

would be expensive because some 10^8 operations would be needed. We use the FFT algorithm instead; thus

$$v_c(\vec{r}) = \tilde{v}_c(\vec{r}) + 4\pi e^2 \left(\frac{Z}{A}\right)^2 \hat{F}^{-1} \frac{1}{|\mathbf{k}|^2} \hat{F}[\rho(\vec{r}) - \tilde{\rho}(\vec{r})]. \quad (2.23)$$

The inverse FFT is similar to Eq. (2.11) except for a change in sign of the exponential and in the normalization. The additional potential $\tilde{v}_c(\vec{r})$ is the one due to the subtraction charge $\tilde{\rho}(r)$ inserted in the FFT to minimize the image problem.¹⁵ We choose $\tilde{\rho}(r)$ as the sum of two spherical Gaussian charge distributions whose individual charges and locations are selected so that $\rho - \tilde{\rho}$ has vanishing net charge, dipole moment, quadrupole, and octupole moment in the principal axis system of the charge quadrupole of ρ . This determines $\tilde{\rho}$ and ensures that the potential due to $\rho - \tilde{\rho}$ goes to zero faster than the usual $1/r$. Then the image problem all but disappears. The Coulomb potential of the Gaussian subtraction charge is, of course, computed exactly as being proportional to $\text{erf}(r/r_s)/(r/r_s)$. The radii of the subtraction charge densities r_s are chosen to yield the correct total rms charge radius for the whole system.

The integration of the equations begins at a separation of 10 fm and usually ends when the fragments have reached a comparable separation. We assume classical Coulomb orbits²³ from $-\infty$ to 10 fm and from the final separation to $+\infty$. The matching to the final Coulomb orbits requires a knowledge of the final masses, charges, separation, and relative momentum vector. These quantities are obtained by straightforward numerical integration over the cluster density and current distributions. An overall check of the TDHF program was performed by selecting an impact parameter large enough to avoid all nuclear interactions. The final computed scattering angle was found to agree with the Coulomb one to 1% at $E/A = 8$ MeV. The exchange Coulomb potential was neglected because it amounts to about 5% of the direct Coulomb potential.

E. Symmetries

The more symmetries we impose on the wave functions, the faster the calculation. However, the fewer the symmetries, the better we compute the thermal energy related to single-particle friction. The present compromise consists in imposing only three symmetries: (i) The quartet symmetry whereby every orbit is spin and isospin saturated and contains four nucleons, (ii) A scattering plane symmetry which assumes that all the wave functions have the form

$$\psi_\lambda(x, y, z) = \pi_s \psi_\lambda(2x_s - x, y, z),$$

where x_s is the location of the y, z scattering plane along the x axis, and π_s is the x parity of the states. This symmetry holds initially and the initial Hamiltonian is even under reflection in the scattering plane. This is not necessarily a stable symmetry, however. Had we started the system with a small violation of this symmetry, the thermalization process might have amplified the deviation from it. (iii) The third symmetry is implemented only in the case of $^{16}\text{O} + ^{16}\text{O}$, where the projectile and target are initially identical. It consists in writing the target wave functions $\psi_\lambda^t(x, y, z)$ as

$$\psi_\lambda^t(x, y, z) = \psi_\lambda^p(x, 2y_{\text{c.m.}} - y, 2z_{\text{c.m.}} - z), \quad (2.24)$$

which reverses the positions with respect to c.m. This also reverses the currents. Because of the scattering plane symmetry (ii) the x variable need not be transformed.

An important question is: What is the effect of these three symmetries on the thermalization? Initially in a real nuclear collision, they hold, of course. The question is then: How fast are these symmetries broken by the thermalization? That is, how fast would the degrees of freedom removed by the symmetry come to thermal equilibrium if they could thermalize? We have run some test cases for $^{16}\text{O} + ^{16}\text{O}$ and it appears that as long as the quartet symmetry is maintained, the symmetries (ii) and (iii) are broken so slowly that by the time we end the collision, they still hold within a few percent. It remains to be seen how the collision would develop if we had only one particle per orbit. We return to this point in the discussion. The quartet symmetry reduces the number of orbits by a factor of 4 and makes the computation nearly four times faster than without it. Similarly, the target-projectile symmetry yields another factor of 2. Finally, the scattering plane symmetry allows a reduction of the number of points in the x direction from 16 to $\frac{16}{2} + 1$.

F. Currents and other fields

The total current $J_\mu(\vec{r})$ can be obtained with the help of the partial FFT, \hat{F}_μ along the μ direction. We have schematically

$$J_\mu(\vec{r}) = \frac{\hbar}{m} \sum_\lambda n_\lambda \text{Im}[\psi_\lambda^*(\vec{r}) \hat{F}_\mu^{-1} k_\mu F_\mu \psi_\lambda(\vec{r})]. \quad (2.25)$$

We have observed that for the cases studied here, the current $J_x(\vec{r})$, along the x direction, e.g., normal to the scattering plane, is generally quite small, so we have set it equal to zero everywhere

We can use the current \vec{J} to compute the total collective kinetic energy:

$$E_{\text{co1}} = \int d^3r \frac{1}{2\rho(\vec{r})} |\vec{J}(\vec{r})|^2. \quad (2.26)$$

This contribution should be subtracted from the total kinetic energy

$$T_{\text{tot}} = \sum_{\lambda} n_{\lambda} \left\langle \psi_{\lambda} \left| \frac{\hbar^2 k^2}{2m} \right| \psi_{\lambda} \right\rangle, \quad (2.27)$$

to obtain an "internal" kinetic energy, E_{int} . This is not yet the thermal energy because we must subtract from E_{int} the Fermi kinetic energy, E_F . The way to find E_F would be to solve the static HF equations constrained to have the instantaneous observed density and take the kinetic energy from that calculation as E_F . This process is time consuming and would require that we use some method similar to the Kohn variational principle²⁴ at every time where we want E_F . We have instead opted for the simpler, but less accurate approximation²⁵

$$E_F(\vec{r}) = A\rho(\vec{r})^{5/3} + B \frac{\hbar^2}{2m} |\vec{\nabla}[\rho(\vec{r})]^{1/2}|^2, \quad (2.28)$$

where the coefficient A is given by

$$A = \frac{3}{5} \frac{\hbar^2}{2m} \left(\frac{3\pi^2}{2} \right)^{2/3} \cong 74.99 \text{ MeV fm}^3, \quad (2.29)$$

and the coefficient B is adjusted at $t=0$ so that $E_F(t=0) = E_{\text{int}}(t=0)$, since there is no heating at that time. The coefficient B was found to be about 0.15 for most cases, a value consistent with theoretical estimates. The total Fermi kinetic energy is the integral of Eq. (2.28) over space, and it is subtracted from E_{int} to give E_{th} , an incoherent kinetic energy, which we take as an approximate thermal energy.

Our thermal and collective energy could be used to define a potential energy as a function of time

$$V \cong E_{\text{tot}} - E_{\text{co1}} - E_{\text{th}}. \quad (2.30)$$

At the beginning of the collision V_i is just the sum of the binding energies of the fragments. At the end of the collision V_f tells us that amount of internal excitation which is even under time reversal. For all cases studied here, $V_f - V_i \geq 0$, and it is of the same order of magnitude as the thermal energy.

III. RESULTS

The results presented in this section are for an ^{14}N projectile incident at 8 MeV/A [$E(^{14}\text{N}) = 112$ MeV] on a ^{12}C target which is to be compared with direct inelastic scattering data¹¹ at 108 MeV. The reaction $^{16}\text{O} + ^{16}\text{O}$ also at 8 MeV/A is shown for comparison with the $^{14}\text{N} + ^{12}\text{C}$ case and with recent²⁶ extensive calculations for $^{16}\text{O} + ^{16}\text{O}$.

A. Density and currents

Figures 1, 2, and 3 show computer-generated displays of the density and velocity distributions for three type of events, vibrational, capture, and rotational scattering. The vibrational example is taken from the $^{14}\text{N} + ^{12}\text{C}$ reaction at 8 MeV/A incident ^{14}N energy and impact parameter $b = 1$ fm. The contour lines in the density plots represent constant values of the integrated density

$$\rho_r(y, z) = \int dx \rho(x, y, z). \quad (3.1)$$

The increment from one contour line to the other is about 0.15 nucleons/fm². The velocity arrows are drawn on the grid points, 1 fm apart, and have been renormalized from one picture to the next to prevent strong overlaps when the velocities are large, or disappearance when they are small. A standard velocity is renormalized by the same amount and is plotted in each frame as a calibration. Only the y and z components of the velocities are shown; the x component was set equal to zero earlier. The values of v_y, v_z in the scattering plane ($x_{\text{c.m.}} = 0$) are shown. The velocity field is obtained from the equation

$$\vec{v}(\vec{r}) = \frac{1}{\rho(\vec{r})} \vec{J}(\vec{r}). \quad (3.2)$$

The first frame of Fig. 1(a), at $t = 30$, begins to show some slight deviation from the starting values of the velocities. The second frame is well into the collision, but not yet past the maximum compression point. We note that the ^{14}N projectile is at the top of the picture at the beginning of the collision. The third frame is only slightly past the maximum compression point. We note that the density never exceeds 1.25 times the equilibrium value. The fourth frame shows the system reconstructing the clusters (vibrational instability). It is also becoming clearer by that frame that the heavy fragment is now at the bottom, and the deflection angle will be about -50 degrees. It would be tempting to inquire further into the penetration process. For example, one might ask whether the two clusters go "through" each other or "bounce" off one another with exchange. Antisymmetrization, however, does not allow a meaningful answer to this question. One might label the orbits that initially belonged to the ^{14}N system and follow them during the scattering. If these orbits end up on the same side, one might claim that the clusters have bounced back while exchanging a nucleon. If they go to the other side, it would appear that they have penetrated one another. This reasoning is, however, incorrect because a single Slater determinant is invariant under any

space-independent unitary transformation among the single-particle orbits. One must rather define a properly observable one- or many-body operator and follow its time dependence. Since the nucleons making up the clusters are identical, such observables must be even under permutation of the particles which form the clusters.

The next four frames at $t=110, 130, 150,$ and 170 fm/c show a persistent neck in the density and an internal octupole vibrational pattern in the velocities. The frame at $t=170$ fm/c shows the velocity in the neck region to be quite high, while the density is small; thus, the neck is snapping off rapidly. This is confirmed in the last frame at $t=190$ fm/c which shows that the neck which has persisted from $t=130$ to $t=170$ fm/c has disappeared in less than 20 fm/c. It is interesting to note that during the $t=140-180$ fm/c period the asymptotic relative motion kinematical properties

are essentially established, yet the two fragments still interact strongly and are changing rapidly with time.

The sequence shown in Fig. 2 comes from the symmetric reaction $^{16}\text{O} + ^{16}\text{O}$ at $E_i/A_p = 8$ MeV, $b = 4$ fm, and comes close to orbiting. The squaring off at $t=80$ fm/c signifies the onset of octupole collective vibration of the fragments. Although the fragments have not quite separated at $t=350$ fm/c, the density in the neck region has dropped considerably, and the momentum of each of the clusters is nearly constant from $t=340$ to $t=350$ fm/c, indicating an eventual breakup.

The last sequence shown in Fig. 3 is intended to illustrate rotational instability, although it is also fairly close to the orbiting value of b . The period from $t=90$ to $t=220$ fm/c shows almost pure rotational scattering, with a slight superimposed octupole vibration of the fragments (hexade-

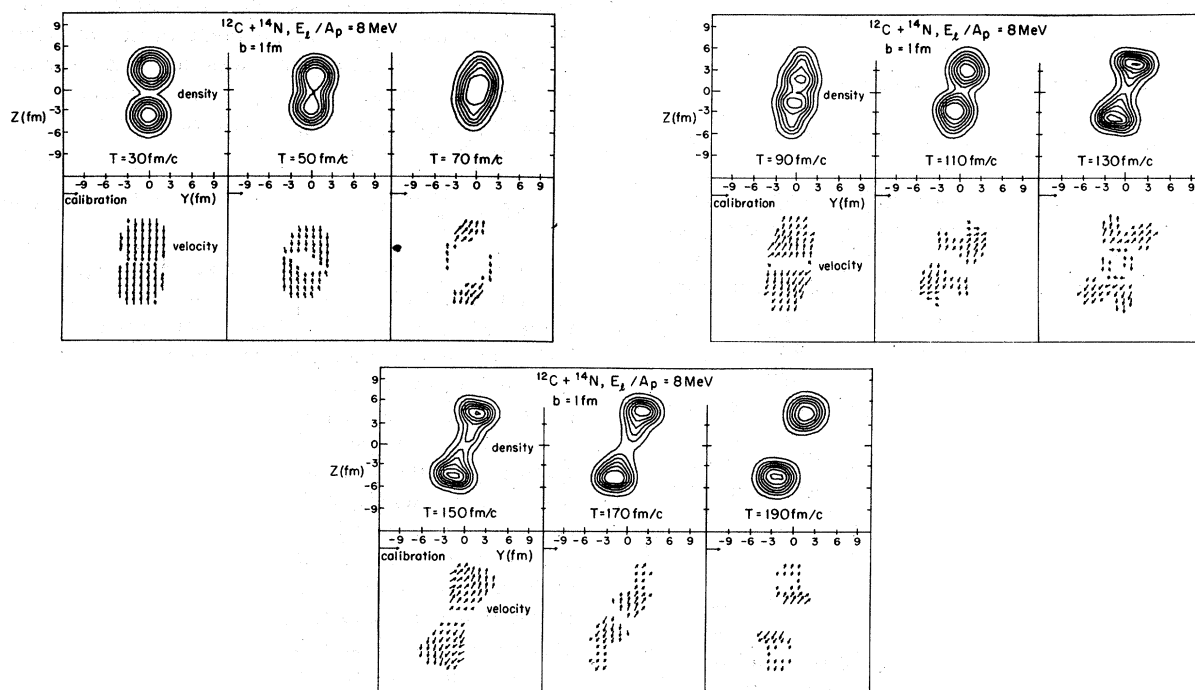


FIG. 1. (a) Density contours for the $^{14}\text{N} + ^{12}\text{C}$ reaction at $E_{\text{lab}}(^{14}\text{N}) = 112$ MeV and at an impact parameter $b = 1$ fm. This sequence of pictures illustrates vibrational instability scattering. The density contours are those of the x -integrated density $\rho_I(y, z) = \int dx \rho(x, y, z)$ and represent steps of about $0.15N/\text{fm}^2$. The velocity field arrows represent the ratio $\vec{J}(\vec{r})/\rho(\vec{r})$, evaluated in the scattering plane ($x_{\text{c.m.}} = 0$) where \vec{J} is the mass current. Each separate velocity frame has an overall normalization constant chosen to display the velocity arrows without overlapping. The calibration arrows show the resulting size of a constant velocity arrow for comparison between frames. Only those arrows which are bigger than some minimum size are displayed, and no arrow is shown in regions where the density is very small. The first frame, at $T = 30$ fm/c, shows the ^{14}N on top. The velocity arrows begin to show a deviation from the initial free motion pattern. By the third frame, at $T = 70$ fm/c, the motion is essentially reversed. (b) Similar to (a), except for $T = 90, 110, 130$ fm/c. The vibrational instability breakup is well under way. The larger fragment is now at the bottom and internal vibrations are apparent. (c) Similar to (a), but for $T = 150, 170,$ and 190 fm/c. The formation of a long neck which persists then snaps off can be observed. The internal oscillations continue after $T = 190$ fm/c.

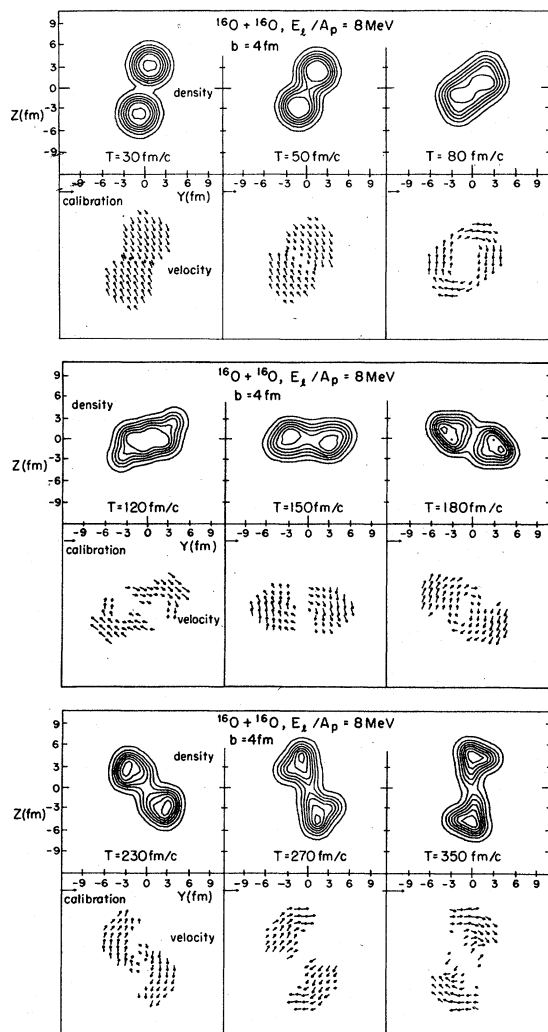


FIG. 2. (a) Densities and velocities for $^{16}\text{O} + ^{16}\text{O}$ at $E_1/A_p = 8$ MeV and impact parameter $b = 4$ fm. This sequence illustrates the near orbiting situation. (b) Similar to (a), but for $T = 120, 150,$ and 180 fm/c. A complex internal vibrational pattern is superposed on the overall rotational pattern. The two ^{16}O clusters are visible at $T = 180$ fm/c and their tetrahedral α structure is also seen. (c) Similar to (a), but for $T = 230, 270,$ and 350 fm/c. The neck is thin in the last frame, but one would have to continue the time development to see if this indicates imminent breakup or if the system will come back together.

capole mode of the compound system). Yet from $t = 220$ fm/c on, elongation sets in and results in separation around $t = 320$ fm/c. In the velocity display of the last frame, we note the presence of octupole vibrations in the fragments. The initial values of the orbital angular momentum for the three cases shown in Figs. 1, 2, and 3 were $l \cong 4\hbar$, $l \cong 20\hbar$, and $l \cong 25\hbar$, respectively. Most of

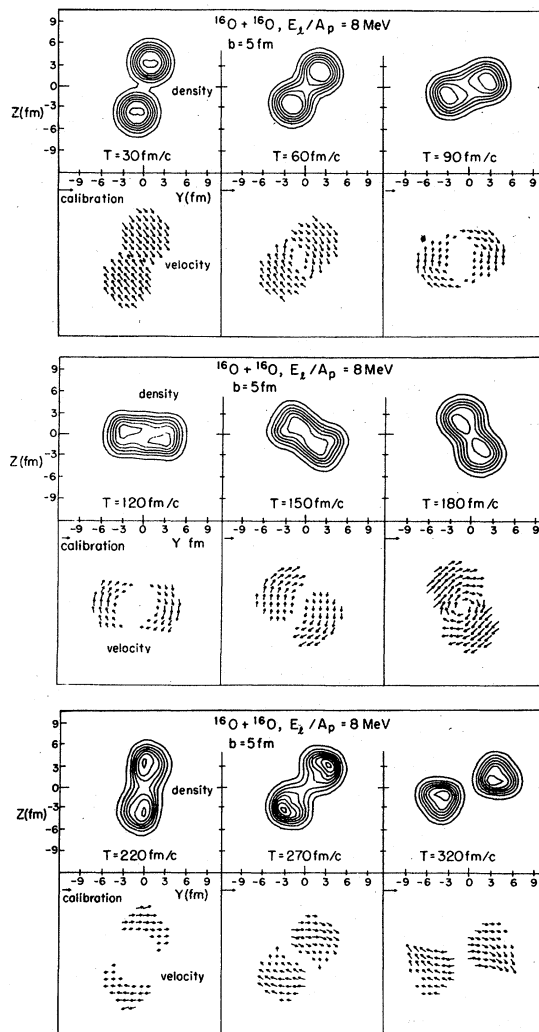


FIG. 3. (a) Densities and velocities for $^{16}\text{O} + ^{16}\text{O}$ at $E_1/A_p = 8$ MeV, and impact parameter $b = 5$ fm. This last sequence illustrates a case of rotational instability. (b) Similar to (a), but for $T = 120, 150,$ and 180 fm/c. One notes the smaller amount of internal vibrations compared to Fig. 2(b), at $b = 4$ fm. (c) Similar to (a), but for $T = 220, 270,$ and 320 fm/c. The neck breaks fairly quickly between $T = 270$ and $T = 320$ fm/c.

the other pictures obtained were similar to the ones shown in these figures and need not be displayed.

These three types of collision show a remarkable similarity with the classical hydrodynamic collisions of liquid drops and this happens in spite of the absence of two-body collision terms which strongly affect the dynamics of classical fluids. Although the single-particle viscosity causes a substantial energy loss, it does not seem large enough to validate the one-fluid theory of hydrodynamics. We have checked that especially at the

higher energies, the Pauli exclusion principle and the single-particle viscosity do not prevent the fragments from penetrating each other so that even in regions where the total current vanishes, the matter is not at rest, but consists of the two fragments "passing through" each other, so that the sum of their individual currents is zero. The density therefore never becomes higher than twice the equilibrium density, as befits a two-fluid model.

B. Dependence on impact parameter

The initial impact parameter b , at $t = -\infty$, is related to the total angular momentum l in the c.m. by

$$l = \mu v b = \hbar k b, \quad (3.3)$$

where $\mu = M_1 M_2 / (M_1 + M_2)$ is the reduced mass and

$$v = \sqrt{\frac{2m E_i}{\hbar^2 A_p}}$$

is the relative velocity of the ions at $t = -\infty$. Most of the calculations reported here were done at $E_i/A_p = 8$ MeV/A, i.e., 128 MeV laboratory energy for the ^{16}O projectile on ^{16}O and 112 MeV laboratory energy for the ^{14}N projectile on ^{12}C . The impact parameter was varied from zero to the value $b = 7.5$ fm where only Coulomb scattering takes place. The deflection function and the outgoing energy vs l are shown in Figs. 4-7. Because of the finite computer budget and the need for smooth functional values from one $[l + \frac{1}{2}]/\hbar$ value to the next, we have done a certain amount of physically reasonable interpolation and extrapolation. Only the points on the curves were obtained from an actual run of the code.

Figure 4 shows the deflection function θ vs the total angular momentum l , for the $^{14}\text{N}+^{12}\text{C}$ case, and Fig. 5 shows the one for $^{16}\text{O}+^{16}\text{O}$. We note that the computer runs were done at different values of l for these two cases in order to obtain as much information as possible. It was apparent from the start that the two cases were qualitatively similar, so the required interpolations were done with this qualitative similarity in mind. These two curves exhibit the well-known behavior of semiclassical deflection functions. There will be a rainbow angle near $l = 28\hbar$ for $^{14}\text{N}+^{12}\text{C}$ and $l = 36\hbar$ for $^{16}\text{O}+^{16}\text{O}$. This angle is also called the grazing angle and is about 9.4° in Fig. 4 and 12.3° in Fig. 5. These are c.m. angles. The conversion to laboratory energies and angles will be given later. A rough estimate is to divide the c.m. angle by 2 to obtain laboratory angles. The change in the sign of θ as l decreases will contribute a glory scattering²¹ and its possible quantum mechanical

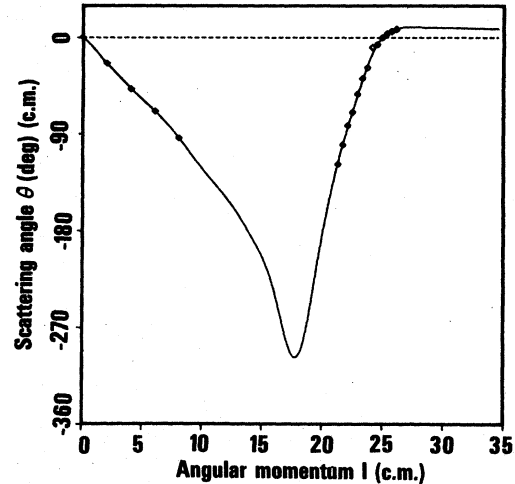


FIG. 4. Deflection function $\theta_{\text{c.m.}}$ vs the incoming orbital angular momentum for the reaction $^{14}\text{N}+^{12}\text{C}$, at $E_{\text{lab}}(^{14}\text{N}) = 112$ MeV. A substantial amount of extrapolation between $l = 8$ and 22 has been performed since actual runs were obtained only for the l values marked with a diamond. The solid line extrapolation was done by hand in order to obtain qualitative agreement with the less expansive curve for $^{16}\text{O}+^{16}\text{O}$ shown in Fig. 5. The deflection function for $l > 25$ is obtained from the pure Coulomb orbits. The grazing angle is $\theta_{\text{c.m.}} \cong 9.4^\circ$, and quasioorbiting occurs around $l = 18\hbar$.

interference with the rainbow is, of course, not included in the present semiclassical approach. The quasioorbiting²¹ value of l is $18\hbar$ in Fig. 4 and around $22\hbar$ in Fig. 5. The occurrence of a single orbiting l value is characteristic of a smooth l -independent attractive potential. Orbiting takes place, for a given bombarding energy, at the angular momentum such that the radial turning point

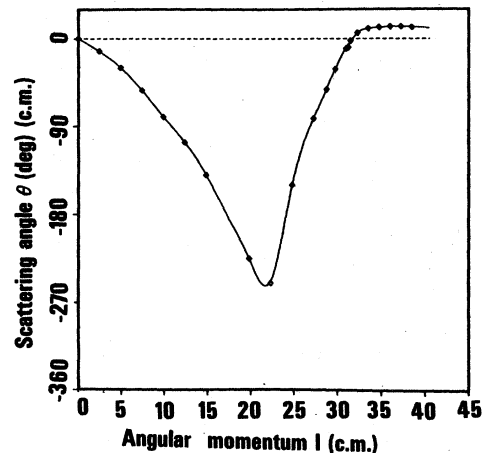


FIG. 5. Deflection function $\theta_{\text{c.m.}}$ vs the incoming orbital angular momentum l/\hbar , for the reaction $^{16}\text{O}+^{16}\text{O}$ at $E_i/A_p = 8$ MeV. This curve and the one of Fig. 4 are similar.

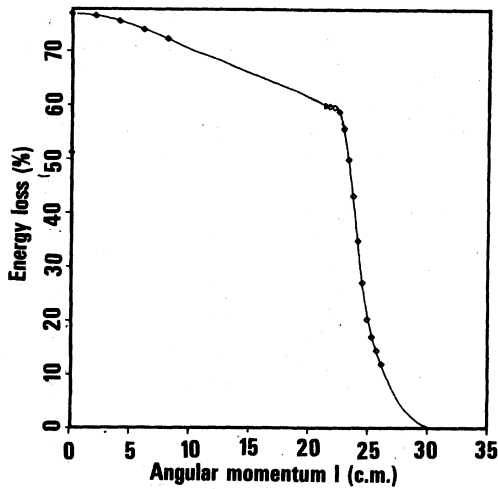


FIG. 6. Percentage relative motion kinetic energy loss vs incoming angular momentum l/\hbar , for the reaction $^{14}\text{N}+^{12}\text{C}$ at $E(^{14}\text{N})=112$ MeV. The squares represent values extracted from computer runs at the appropriate impact parameter, while the dashed and solid curves are extrapolations drawn by hand and designed to make Figs. 6 and 7 similar.

occurs for an effective potential

$$+ \frac{\hbar^2 l(l+1)}{2m r^2} + V(r)$$

which has zero first derivative at the turning point. We are not suggesting that the effective potential is that simple, since the orbiting cusp is clearly damped in these two figures. Nevertheless, it is satisfying to recognize familiar elements of potential scattering in the present context. The small l value deflection angle in Fig. 5 could be made to approach 180° instead of zero degrees since the

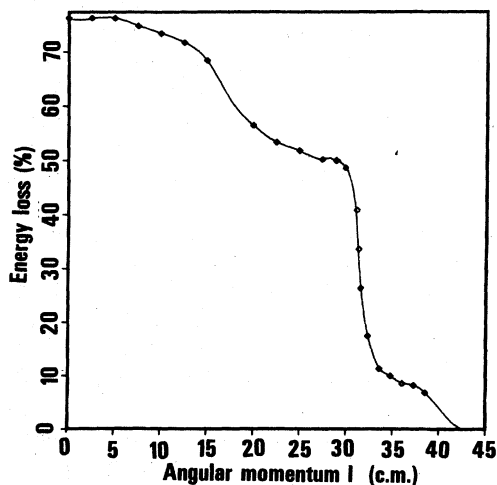


FIG. 7. Similar to Fig. 6, but for $^{16}\text{O}+^{16}\text{O}$ at $E_l/A_p = 8$ MeV.

clusters are indistinguishable. We have selected the zero degree limit in order to obtain a curve similar to the one of Fig. 4.

Figure 6 shows the percentage c.m. energy loss during the collision for $^{14}\text{N}+^{12}\text{C}$. The initial c.m. relative motion kinetic energy is 51.69 MeV. The biggest fraction of the energy loss occurs before one reaches the orbiting value of angular momentum. The energy loss in the vibrational instability region has a much weaker dependence on the l value. It is interesting to note that the outgoing relative motion kinetic energy does not seem to bear any direct relation to the Coulomb plus rotational energy formula one might expect from a strongly damped collision.³ This may be due to the ambiguity in defining a moment of inertia. The experimental results in the case⁵ of $^{20}\text{Ne}+^{27}\text{Al}$, however, appear to obey the Coulomb plus rotational limit. It may be that the present reaction does not exhibit enough friction, perhaps because the fragments are too light, to dampen the velocity field into a simple rotational mode. Some evidence for additional nonrotational components to the velocity field is indeed present in Figs. 1-3. It is unfortunate that the quantum effects make it difficult to observe directly the energy loss as a function of angular momentum for such a light system as the present one.

Figure 7 shows the percentage kinetic energy loss for the $^{16}\text{O}+^{16}\text{O}$ reaction. There the initial c.m. relative motion kinetic energy is 64 MeV. The main component of the loss again occurs just above the orbiting l value but it is now accompanied by other kinks at higher and lower l values. Although this is one of the few well-defined qualitative differences between the two reactions studied here, it may not be very important for the following reason. We recall that the initial wave functions are harmonic oscillator states and not self-consistent states. The clusters therefore develop some internal motion before they come in contact. This motion may be different for the two cases here and can account for the differences at high l 's. To understand the difference at low l 's, we must keep in mind that the initial relative motion translational kinetic energy is stored, during the collision, as a collective kinetic energy field, as illustrated by the velocity field in Figs. 1-3. At the end of the collision, not all of the remaining velocity field is converted to pure translational motion. Some vibrational and rotational energy remains inside the clusters. The partition between these modes depends, to a certain extent, on the details of the velocity field at the instant where the neck snaps off. After that, conservation of momentum ensures the constancy of $E_k(\text{rel})$. The additional kinks at low l 's could therefore be due

TABLE I. Energy dependence of $^{16}\text{O} + ^{16}\text{O}$ reaction at $b = 4$ fm.

E_l/A_p ^a (MeV)	k_{sp} ^b (fm ⁻¹)	t^* ^c (fm/c)	$\hbar k_{sp} t^*/m$ (fm)	$\rho_{IC}(t^*)$ ^d (N/fm ²)	$R_{rms}(t^*)$ ^e (fm)	t_f (fm/c)	$\rho_{IC}(t_f)$ ^f (N/fm ²)	Cluster			E_{kin} c.m.	E_{th} (MeV), $t = t_f$	E_{col}
								separation at $t = t_f$ fm	θ_{scat} (deg)	$R_{rms}^{int}(t_f)$ ^h			
4	0.439	130	12.0	0.77	3.56	370	0.664	4.86	-108 ^g	2.71	5.5	21	12.5
6	0.539	100	11.4	0.79	3.54	300	0.285	7.37	-83 ^g	2.80	6.5	20	10.9
8	0.621	80	10.5	0.74	3.54	350	0.273	8.29	-106 ^g	2.96	7.3	28	11.4
12	0.761	60	9.7	0.72	3.53	250	0.521	5.53	-120 ^g	3.13	21	51	32
18	0.932	40	8.0	0.73	3.50	180	0.586	6.20	-195 ^g	3.33	28	70	43
24	1.076	40	8.8	0.76	3.45	210	0.009	11.8	-135	3.54	29	99	43
36	1.318	30	8.4	0.77	3.41	100	0.050	11.8	-44	3.46	84	102	120

^a Value at $t = -\infty$; when the calculation begins at $t = 0$ and a separation of 10 fm, the Coulomb energy $E_{coul} = 9.2$ MeV is subtracted from the c.m. energy $8 E_l/A_p$.

^b We use $E_l/A_p = \hbar^2/2mk_{sp}^2$, $m =$ single nucleon mass.

^c Time needed to reach the minimum rms radius.

^d Central density integrated along the x axis; the initial equilibrium value inside a cluster is 0.915 N/fm².

^e Total rms radius with respect to the c.m. of the full distribution.

^f Complete separation has been attained only for the last two energies.

^g Will continue to rotate before coming apart.

^h Internal rms radius of each cluster with respect to its c.m. $R_{rms}^{int}(t=0) = 2.5$ fm.

to fluctuations in the amount of internal collective energy at scission.

We have mentioned in Sec. II that the thermal and collective energies are also calculated as a function of time and orbital angular momentum. We do not display them explicitly here; instead we comment briefly on their dependence on l . To first order, the thermal energy $E_{th}(l)$ is about 60% of the actual energy loss, for most values of l . Thus, for $l = 0$, and $^{14}\text{N} + ^{12}\text{C}$, where the energy loss is about 40 MeV, some 24 MeV of this is accounted for by the thermal energy. Another 10% of the energy loss, i.e., 4 MeV at $l = 0$, is found as internal collective energy of the two fragments. This leaves us with about 12 MeV of unaccounted energy loss. This amount might be explained by the fact that the radii of the fragments are substantially greater as they emerge from the collision than they were before. The nuclear potential energy should, therefore, be less attractive. The surface thickness is also increased so that Eq. (2.25) would predict a somewhat higher Thomas-Fermi kinetic energy. Thus, the stationary part of the nuclear bound state energy is decreased with respect to the initial system. We presume that a loss of binding of 6 MeV per cluster can be accounted for in this way. In any case, this number is subject to a sizable uncertainty because of the fairly large absolute errors in the estimate, Eq. (2.25), needed for the computation of E_{th} . The amplitudes shown in Figs. 6 and 7 will be mentioned in the discussion. Subsection D will use the present results for $\theta(l)$ and $E(l)$ to construct angular distributions in the laboratory system.

C. Energy dependence

It would be desirable to compute curves of $\theta(l)$ and \bar{E}_T over a wide range of incident energies. A more limited exploration of the energy dependence of the reaction is given in Table I. The values $E/A = 4, 6, 8, 12, 18, 24$, and 36 MeV/A are represented, using an impact parameter b of 4 fm. This table qualitatively complements the one obtained at $b = 0$ for the $^{12}\text{C} + ^{12}\text{C}$ reaction.¹⁸

The main result of this study is that one must go to energies of the order of 20 MeV/A before one observes a clear disappearance of the near orbiting phenomenon at $b = 4$. For the head-on collision of $^{12}\text{C} + ^{12}\text{C}$, capture occurs only at $E/A < 6.8$ MeV. The first column of Table I gives the energy per nucleon of the ^{16}O projectile in the laboratory system and the second column gives the corresponding single-particle momentum. The time t^* , given in the third column, is the one at which the total rms radius R_{rms} with respect to the c.m. of the complete distribution is at a minimum (column 6). This radius decreases slightly with increasing bombarding energy. It never comes close to the ground state radius of the $A = 32$ system, $R = 3.15$ fm. Another indication of the near total lack of compression at these energies is seen from the x -integrated central density given in column 5. It fluctuates around 0.75 N/fm², which is smaller than the starting value of 0.91 N/fm². Column 4 gives the equivalent change in the cluster separation in going from $t = 0$ to $t = t^*$. The average value of these is 9.8 fm and is close to the actual initial separation of 10 fm. The greater value at the lower energies indicates

that the orbit deviates from a straight line. The smaller value at higher energy shows a more direct trajectory indicating some finite size effect. The relatively constant value of the equivalent change indicates that the geometry of the trajectories, until the minimum compression point is reached, scales fairly well with the incoming velocity. This conclusion was also reached for head-on collisions¹⁸ over a still greater range of energies and with a quite different interaction.

The final time at which the collision is frozen was chosen somewhat arbitrarily to conserve computing time and to accommodate the available runs. The integrated central density, the cluster separation distances, and the scattering angle, columns 8, 9, and 10, give an idea of how far the collision has proceeded by that time. Most of the thermalization takes place during a time interval centered around t^* . Thus the internal rms radius of a cluster given in column 11 should be reliable. The initial value was 2.50 fm. The increase is mainly due to the thermal energy given in column 13. There is an increase of about 0.5 fm for each 50 MeV of thermal excitation. One can obtain an estimate for the total internal energy of the fragments by subtracting the kinetic energy of relative motion E_{kin} (column 12) from the initial Coulomb subtracted collective energy ($8 E/A_p - 9.2$ MeV). This is the Q value of the reaction and ranges from 16 MeV at low energy to about 194 MeV at high energy. The last column gives the final collective energy $E_{col1}(t_f)$. This value includes the relative motion kinetic energy of column 12. $E_{col1} - E_{kin}$ is the total internal collective energy and varies from 7 to 36 MeV. Some of this energy is internal rotational energy but most of it is octupole and higher multipole vibrational energy. The thermal energy column 13 is unfortunately somewhat unreliable due to the difficulty of estimating the ground state energy for the instantaneous density configuration at $t=t_f$. This ground state energy at fixed density could be obtained from the Kohn variational principle, but our present implementation of it was an iterative procedure which was too time consuming²⁴ to be practical.

As in the case of head-on collisions, the behavior of the collision after the minimum radius time does not scale with the incoming velocity. At the higher energies, the trajectory straightens as expected while at low energies orbiting appears to take place.

D. Inelastic scattering angular distributions

The deflection curves obtained earlier can be used in the classical physics formula²³

$$\frac{d\sigma}{d\Omega} = \left| \frac{b db}{\sin\theta d\theta} \right| \quad (3.4)$$

appropriate for the classical way in which the TDHF method treats the orbits of the clusters. The curve for $db/d\theta$ can be obtained from the deflection function $d\theta/dl$ and the Eq. (3.3). The deflection functions given in Figs. 4 and 5 are in the c.m. system so that a c.m. differential cross section would be obtained if we used these curves directly. However, by using the curve for \bar{E}_1 and the classical conversion from c.m. angles to laboratory angles, it is easy to obtain the laboratory deflection function $\theta_{lab}(l_{tot})$. The impact parameter b remains the same and Eq. (3.4) can now be used by taking θ to be the laboratory angle. The kinematic equations then limit θ_{lab} to be less than about 35° because of the large energy loss and the fact that the heavy fragment is the projectile. The resulting curve for $d\sigma/d\Omega$ has several branches which are shown in Fig. 8. The branch labeled (1) in the figure corresponds to the region from the grazing angle to $\theta=0$, e.g., l values from

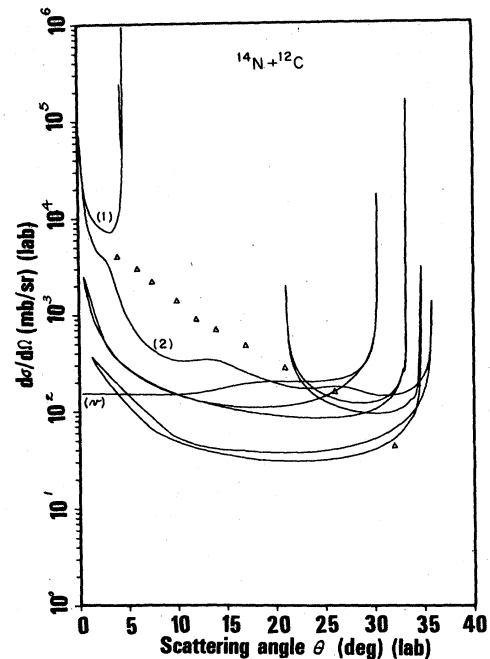


FIG. 8. Predicted classical direct inelastic scattering cross section of $^{14}\text{N}(E_{lab} = 112 \text{ MeV})$ on ^{12}C in the TDHF approximation vs laboratory angle θ_{lab} . The branch marked (1) represents positive angle scattering up to the grazing angle. The branch marked (2) represents negative small angle scattering. This branch folds back and forth several times at lower values because of the kinematics of a heavy projectile undergoing large energy losses. The branch marked (ν) represents small negative angle vibrational scattering. The triangles are data points taken at ORNL at $E_{lab}(^{14}\text{N}) = 108 \text{ MeV}$. The data are summed over inelastic energies and final charge values of the outgoing heavy fragment (see Ref. 28).

24.5 to $27\hbar$ in Fig. 4. The singularities in the various branches at $\theta_{\text{lab}} = 0$ come from the $1/\sin\theta$ term. The other singularities occur whenever $d\theta_{\text{lab}}/db$ has a zero. The second branch, marked (2) in the figure, has mainly a $1/\sin\theta$ dependence. The kinks in that branch come mainly from the irregularities in interpolating the calculated points in Figs. 4 and 5. The last branch, marked (v) in Fig. 8, represents vibrational instability scattering. Since the deflection function is nearly linear vs l for small l , the $1/\sin\theta$ singularity in that branch is canceled and vibrational instability scattering is nearly isotropic. The triangles shown in Fig. 4 represents data obtained¹¹ at Oak Ridge National Laboratory for the direct inelastic scattering of 108 MeV ^{14}N ions on ^{12}C . This cross section is the sum over all reaction products with energy less than the elastic peak and greater than about one-half the elastic energy. The data have also been summed over the Z values 6, 7, 8, 9 of the reaction products. The main characteristic of these data is a nearly constant exponential decay with increasing laboratory angle characteristic of reactions with lighter projectiles.⁵⁻¹⁰ The theory curve is seen to resemble this exponential curve only vaguely.

A second, and perhaps more important, discrepancy between theory and experiment is the observation that if we sum over all branches and integrate over $\sin\theta d\theta$ the resulting theoretical direct inelastic cross section is too high, at about 1500 mb, compared to the corresponding experimental one (~650 mb). The total experimental fusion cross section at this energy^{6,11} is 890 ± 100 mb, for a total experimental reaction cross section of about 1540 mb. Thus, the present calculation errs, in that it has no fusion region and too much direct inelastic scattering, but it predicts a reasonable value for the total reaction cross section. The lack of fusion in the present calculation can be understood in the light of recent results²⁶ using a self-consistent initial state and a finite-range two-body component on the interaction. Here we have used a zero-range interaction and a non-self-consistent harmonic oscillator initial state. These two changes appear to have a substantial influence on the behavior of the fusion window vs energy. Thus, for $^{16}\text{O} + ^{16}\text{O}$ at 6.46 MeV, Flocard²⁶ *et al.* find a fusion cross section of 840 mb corresponding to complete fusion between the l values of 13 and $27\hbar$. The differential cross section for $^{16}\text{O} + ^{16}\text{O}$ is shown in Fig. 9 and is similar to the one shown in Fig. 8 for $^{14}\text{N} + ^{12}\text{C}$.

IV. DISCUSSION

We have presented in this paper a calculation of the direct inelastic scattering of ^{14}N by ^{12}C at

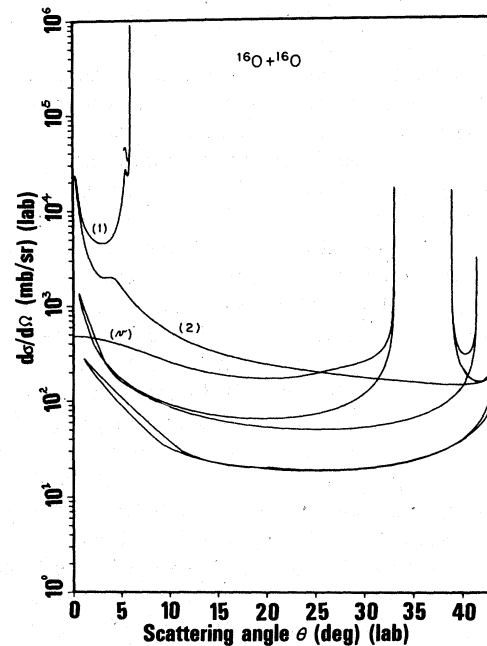


FIG. 9. Similar to Fig. 8 except for $^{16}\text{O} + ^{16}\text{O}$ at $E_{\text{lab}}(^{16}\text{O}) = 128$ MeV.

112 MeV and ^{16}O by ^{16}O at 128 MeV. We have also explored the energy dependence of the $^{16}\text{O} + ^{16}\text{O}$ reaction at an impact parameter of 4 fm. We have used the TDHF formalism to obtain the deflection function as a function of incident (total) angular momentum. A brief derivation of the equations of the TDHF method was given in order to bring out the three main approximations made: (i) neglect of two-body correlations, (ii) simplification of the interaction, and (iii) a filling approximation for the density which reduces to a single Slater determinant for closed-shell nuclei. We have also used harmonic oscillator initial states. As a result of the zero-range simplified interaction and the use of harmonic oscillator states, the fusion cross section predicted by TDHF is zero. Thus, all the incident flux is concentrated in the direct inelastic channels so that when we compare the predicted cross section for these channels with data at 108 MeV for $^{14}\text{N} + ^{12}\text{C}$, we find an integrated theoretical cross section which is too large by nearly a factor of 2 and a theoretical angular distribution which only poorly resembles the observed exponential drop with laboratory scattering angle. The introduction of an L -dependent fusion window would allow us to reproduce the observed fusion cross section and would lower the predicted inelastic cross section, as discussed in Ref. 27. This last reference also gives results for finite range forces.

There are other corrections besides those due

to fusion which should be applied. They are quantum mechanical in nature and result from time-energy and angle-angular momentum uncertainties. The comparison with experiment also requires that one do an evaporation calculation on the fragments emerging from the reaction. These calculations go far beyond the TDHF method and will be reported elsewhere.²⁸ The complete justification for the quantal corrections is expected to come from more basic reaction theory.²⁹ However, a phenomenological formulation of the corrections used in Refs. 27 and 28 has been given³⁰ and does appear to predict final results for Z distribution, energy, and angular distributions in the

reaction $^{14}\text{N}(112\text{ MeV}) + ^{12}\text{C}$ which are in good agreement with experiment. Thus it seems that one needs self-consistent initial states and finite range forces in the pure TDHF portion of the calculation in order to reproduce fusion cross sections, while one has to go considerably beyond TDHF to compare angular, energy, and charge distributions with experiment.

We acknowledge stimulating discussions of the present work with Dr. R. G. Stokstad, J. Gomez del Campo, J. W. Negele, S. E. Koonin, and the members of the Theory Group of the Physics Division at Oak Ridge National Laboratory.

*Consultant to Physics Division. Oak Ridge National Laboratory, Oak Ridge, Tennessee 37830.

†Present address: Institut für Theoretische Physik, Universität Frankfurt, Frankfurt, West Germany.

‡Research sponsored by the Division of Physical Research, U. S. Department of Energy, under Contract No. W-7405-eng-26 with the Union Carbide Corporation.

§Work performed under the auspices of the U. S. Department of Energy by the Lawrence Livermore Laboratory under Contract No. W-7405-ENG-48.

¹M. Lefort, C. Ngô, J. Péter, and B. Tamain, Nucl. Phys. **A216**, 166 (1973).

²F. Hanappe *et al.*, Phys. Rev. Lett. **32**, 738 (1974); K. L. Wolf *et al.*, *ibid.* **33**, 1105 (1974).

³R. Vandenbosch, M. P. Webb, and T. D. Thomas, Phys. Rev. Lett. **36**, 459 (1976); Phys. Lett. **62B**, 407 (1976).

[See also *Classical and Quantum Mechanical Aspects of Heavy Ion Collisions*, edited by H. L. Harvey *et al.* (Springer, Berlin, 1975)].

⁴K. Siwek-Wilczynska and J. Wilczynski, Nucl. Phys. **A264**, 115 (1976).

⁵R. Eggers, M. N. Namboodiri, P. Gonthier, K. Geoffroy, and J. B. Natowitz, Phys. Rev. Lett. **37**, 324 (1976).

⁶R. G. Stokstad, J. Gomez del Campo, J. A. Biggerstaff, A. H. Snell, and P. H. Stelson, Phys. Rev. Lett. **36**, 1529 (1976).

⁷J. M. Cormier *et al.*, Phys. Rev. C **13**, 682 (1976).

⁸J. Natowitz, M. N. Namboodiri, and E. T. Chulick, Phys. Rev. C **13**, 171 (1976); Nucl. Phys. **A263**, 491 (1976).

⁹P. Sperr *et al.*, Phys. Rev. Lett. **37**, 321 (1976).

¹⁰K. G. Nair *et al.*, Phys. Rev. C **12**, 1575 (1975).

¹¹R. G. Stokstad *et al.*, Phys. Lett. **70B**, 289 (1977).

¹²J. S. Blair, in *Lectures in Theoretical Physics*, edited by P. D. Kunz and W. E. Brittin (University of Colorado Press, Boulder, 1966), Vol. VIII-C, pp. 343-444.

¹³R. C. Singleton, IEEE Trans. Audio Electroacoust. **17**, 93 (1969).

¹⁴I. S. Berezin and N. P. Zhidkov, *Computing Methods* (Pergamon, New York, 1965), Vol. II, p. 352 ff.

¹⁵J. A. Maruhn, T. A. Welton, and C. Y. Wong, J. Com-

put. Phys. **20**, 320 (1976).

¹⁶P. A. M. Dirac, Proc. Cambr. Philos. Soc. **26**, 376 (1930).

¹⁷R. Y. Cusson, R. K. Smith, and J. A. Maruhn, Phys. Rev. Lett. **36**, 1166 (1976).

¹⁸J. A. Maruhn and R. Y. Cusson, Nucl. Phys. **A270**, 437 (1976).

¹⁹P. Bonche, S. E. Koonin, and J. W. Negele, Phys. Rev. C **13**, 1226 (1976); S. E. Koonin, Phys. Lett. **61B**, 227 (1976); S. E. Koonin, K. T. R. Davies, V. Maruhn-Rezwani, H. T. Feldmeier, S. J. Krieger, and J. W.

Negele, Phys. Rev. C **15**, 1359 (1977); V. Maruhn-Rezwani, K. T. R. Davies, and S. E. Koonin, Phys. Lett. **67B**, 134 (1977).

²⁰R. A. Broglia, S. Landowne, R. A. Malfliet, V. Rostokin, and Aa. Winther, Phys. Rep. **11C**, 1 (1974).

²¹K. W. Ford and J. A. Wheeler, Ann. Phys. (N.Y.) **7**, 259 (1959).

²²M. Born and H. S. Greene, *A General Kinetic Theory of Liquids* (Cambridge University Press, Cambridge, England, 1949).

²³H. Goldstein, *Classical Mechanics* (Addison-Wesley, Reading, Mass., 1950).

²⁴P. Hohenberg and W. Kohn, Phys. Rev. **136**, B864 (1964).

²⁵C. Y. Wong (private communication).

²⁶P. Bonche, B. Grammaticos, and S. E. Koonin, Phys. Rev. C **17**, 1700 (1978); H. Flocard, S. E. Koonin, and M. S. Weiss, *ibid.* **17**, 1682 (1978).

²⁷R. Y. Cusson, J. Gomez del Campo, and H. W. Meldner, in *Proceedings of the Third International Conference on Clustering in Nuclei* (University of Manitoba Press, Winnipeg, Canada, 1977).

²⁸R. Y. Cusson, J. Gomez del Campo, and J. A. Maruhn (unpublished).

²⁹J. Knoll and R. Schaeffer, Phys. Rep. **31C**, 159 (1977).

³⁰R. Y. Cusson, Proceedings of the Fall Creek Falls Conference on Heavy Ion Collisions, 1977, Report No. CONF-770602 (unpublished); J. A. Maruhn, R. Y. Cusson, and H. W. Meldner, in Proceedings of the Ljubliana Conference on Heavy Ions, Ljubliana, Yugoslavia, 1977, Fizika **9**, 291 (1977).